

# **Supplementary Information: Solution-processed PbS quantum dot infrared laser with room-temperature tuneable emission in the optical telecommunications window**

G. L. Whitworth,<sup>1</sup> M. Dalmases,<sup>1</sup> N. Taghipour,<sup>1</sup> G. Konstantatos<sup>1,2,\*</sup>

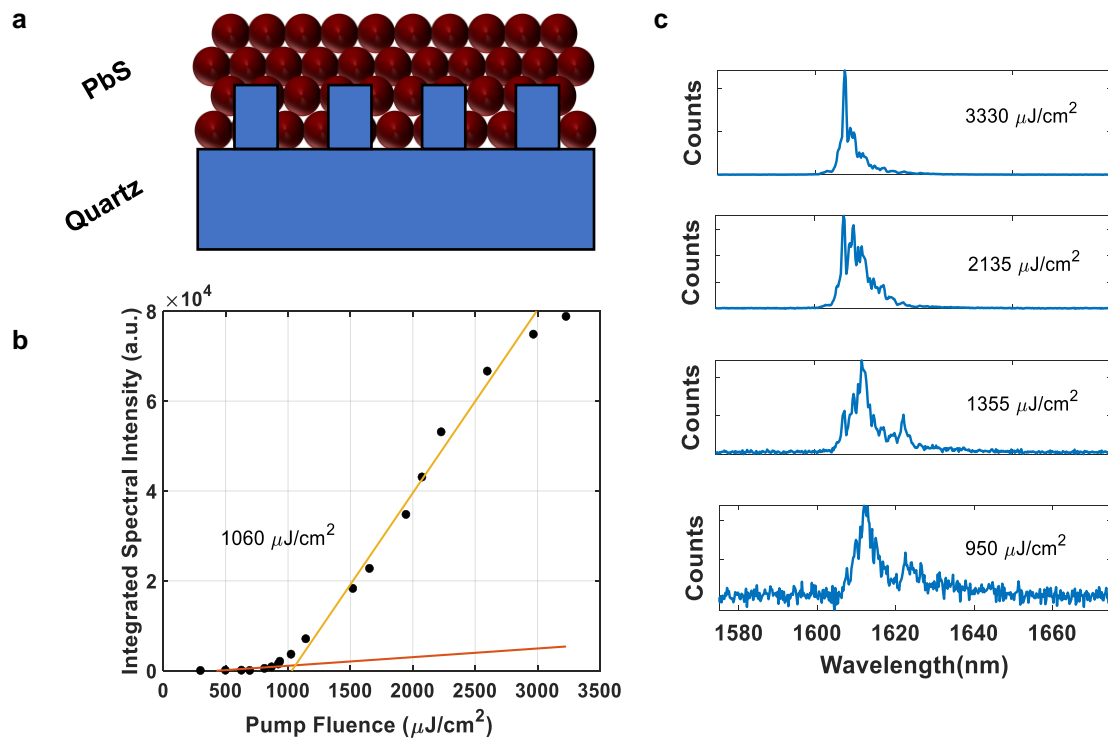
<sup>1</sup> *ICFO, Institut de Ciències Fòniques, The Barcelona Institute of Science and Technology, 08860 Barcelona, Spain*

<sup>2</sup> *ICREA, Institució Catalana de Recerca i Estudis Avançats, 08010 Barcelona, Spain*

\*Gerasimos.konstantatos@icfo.eu

## I. Quartz Grating PbS DFB lasing

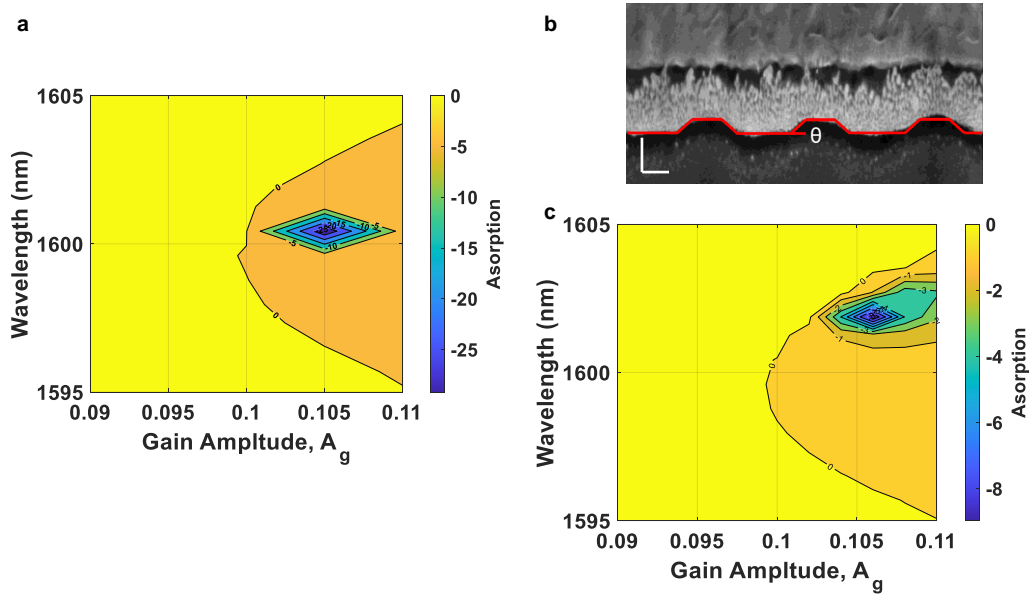
Quantum dot lasers were initially fabricated using quartz substrate gratings (Fig. 1a). However, when using quartz stable, narrow line-width DFB lasing was not easily achievable. As seen in Supplementary Information Fig. S1b & S1c, around laser turn-on threshold ( $1060 \mu\text{J}/\text{cm}^2$ ) the emission spectra was broad (FWHM  $\sim 10 \text{ nm}$ ) and centred at  $1612 \text{ nm}$ . With increasing power, narrow random-like laser peaks could be seen to appear along with a blue shift in the spectra. At high pump fluences a narrow peak (FWHM  $\sim 1 \text{ nm}$ ) at  $1607 \text{ nm}$  appeared, potentially indicating DFB lasing arising as the gain spectrum blue shifted across the gain spectrum. The intensity of the blue shifting effect was noticed to be dependent on the repetition rate of the laser and therefore was prescribed to a heating effect. As such, the switch was made to sapphire substrates which has a roughly 20 times higher thermal conductivity, in order to achieve stable lasing.



**Supplementary Figure 1. PbS DFB structures using quartz gratings.** (a) Schematic of PbS quantum dots on top of a quartz grating fabricated in the same manner as described in Methods. (b) Integrated spectral intensity plotted against incident pump fluence with linear fits above and below threshold with the calculated threshold shown. (c) Stacked plot of emission spectra collected from quartz grating PbS DFB samples for four different pump fluences as indicated.

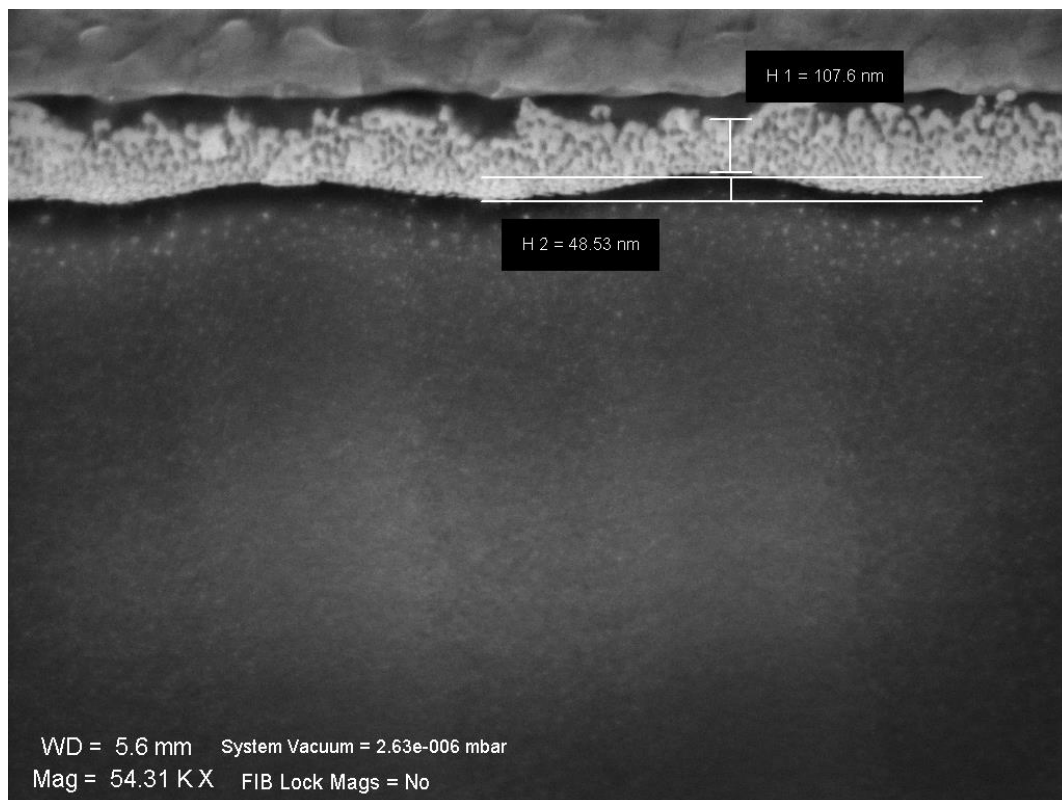
## II. Extended plot of variable gain model

Using the variable gain FDFD model we can calculate the absorption of the DFB structures as a function of wavelength and gain amplitude,  $A_g$ , to predict the existence of DFB lasing modes. When a rectangular grating shape was assumed, as shown in Fig. 1, a lasing mode appears at 1600 nm and  $A_g = 0.105$  in wavelength-gain space (Fig. S2a). However, when fabricated, gratings were seen to have a  $20^\circ$  side-wall angle, and curved edges. To check if the model still successfully predicts laser to appear in the real fabricated structures a trapezoidal approximation was made of the gratings as shown in Fig. S2b and input into the FDFD model. These results shown in Fig. S2c shows that the trapezoidal structures still predict lasing but with a red shift of 2 nm.



**Supplementary Figure 2. Absorption from variable gain FDFD model.** (a) A contour plot of the simulated absorption of the rectangular structure as shown in Fig. 1c,d, as a function of wavelength and gain amplitude. The transparency contour (absorption = 0) is indicated and areas of negative absorption indicates gain in the system. (b) The cross-sectional FIB image from figure 1(g) with an trapezoidal red overlay, indicating a period of 885 nm, a 210 nm top grating width, and a  $20^\circ$  side-wall angle  $\theta$ . (c) Resultant absorption from FDFD modelling as in (a), when the trapezoidal structure from (b) is used.

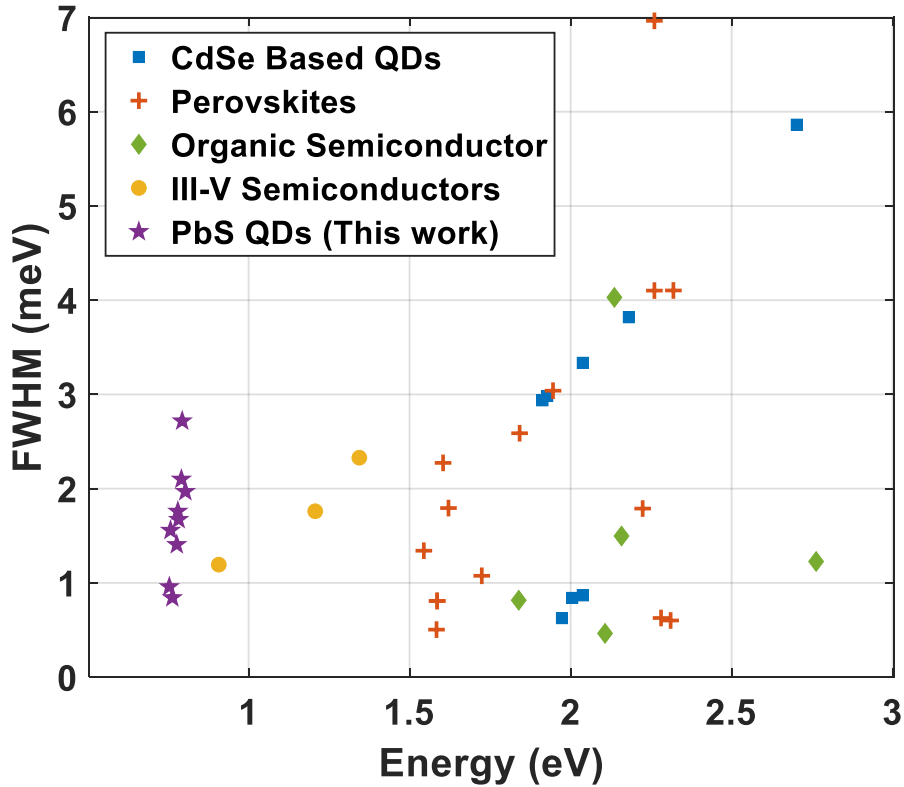
### III. Grating and DFB structural characterisation



**Supplementary Figure 3. SEM measurements of FIB milling.** An angled SEM image of the PbS grating shown in Fig 1g with added measurements of the grating height and PbS thickness

#### IV. Line-width Comparison and Discussion

We have performed a literature search on semiconductor DFB lasers of similar materials and linewidths tend to fall between 0.1 and 1 nm as plotted in. However as these mainly operate in the visible, it is the linewidth in energy which is a better figure of merit in order to compare the DFB lasers. As can be seen from Fig. S12 linewidths range typically from 0.5 meV to 4 meV. Our lasers compare well, with linewidths in the range 1 meV to 2 meV.



**Supplementary Figure 4. Linewidth Comparison.** FWHM of a selection of DFB lasers found in the literature plotted against their central lasing energy. References for each point can be found in Table S1.

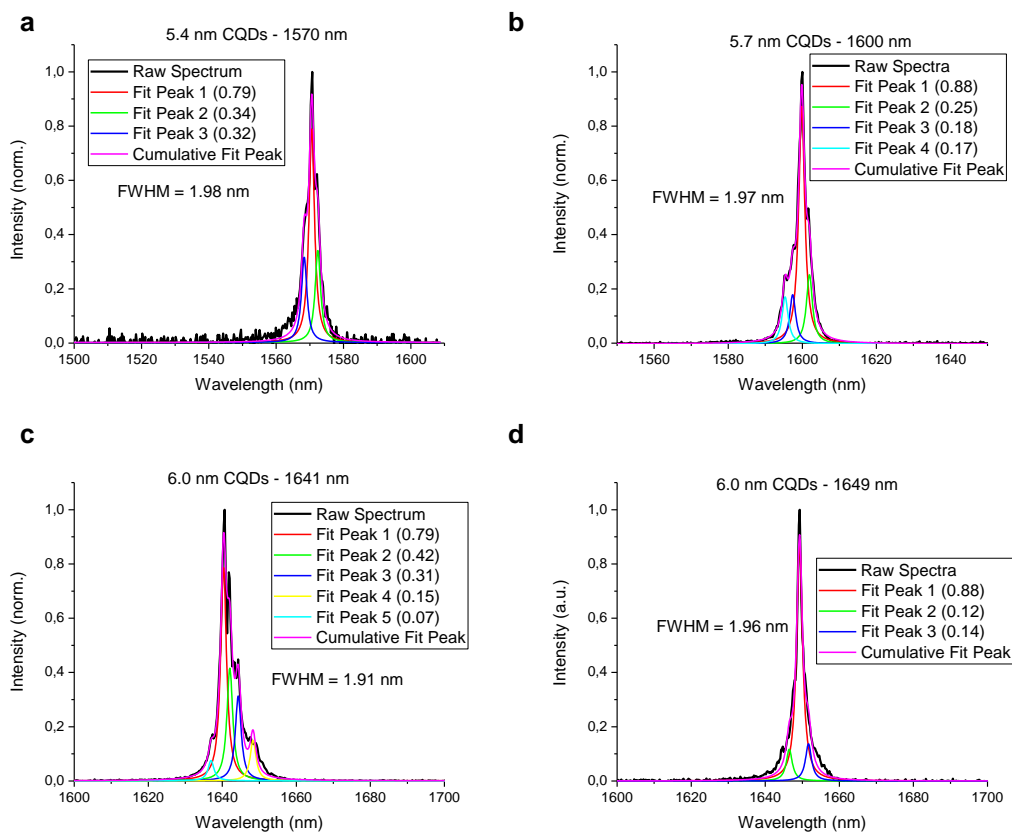
Table S1: Reference table of data presented in Fig. S4

Active Medium	Wavelength (nm)	FWHM (nm)	Energy (eV)	FWHM (meV)	DOI
CdSe	570	1.00	2.18	3.83	10.1364/OE.22.018800
CdSe	460	1.00	2.70	5.89	10.1364/OE.22.018800
CdSe	610	1.00	2.04	3.35	10.1364/OE.22.018800
CdSe	610	0.26	2.04	0.87	10.1063/1.4826147

CdSe	620	0.26	2.01	0.84	10.1063/1.4826147
CdSe	650	1.00	1.91	2.95	10.1002/adfm.201101684
CdSe	645	1.00	1.93	2.99	10.1021/acsami.7b01669
CdSe	630	0.20	1.97	0.63	10.1126/science.aax3489
Perovskite	805	0.70	1.54	1.34	10.1021/acsnano.8b04854
Perovskite	550	1.70	2.26	7.01	10.1002/adma.201906571
Perovskite	550	1.00	2.26	4.12	10.1038/s41598-017-11569-3
Perovskite	775	1.10	1.60	2.28	10.1021/acs.nanolett.6b01946
Perovskite	785	0.25	1.58	0.50	10.1038/s41566-017-0047-6
Perovskite	559	0.45	2.22	1.79	10.1038/s41586-020-2621-1
Perovskite	784	0.40	1.59	0.81	10.1364/OE.26.00A144
Perovskite	545	0.15	2.28	0.63	10.1021/acsphotonics.7b00780
Perovskite	538	0.14	2.31	0.60	10.1002/adma.201903717
Perovskite	536	0.95	2.32	4.12	10.1021/acsphotonics.9b01501
Perovskite	721	0.45	1.72	1.08	10.1021/acsphotonics.9b01501
Perovskite	767	0.85	1.62	1.80	10.1021/acsphotonics.9b01501
Perovskite	639	1.00	1.95	3.05	10.1021/acsphotonics.9b01501
Perovskite	675	0.95	1.84	2.60	10.1021/acsphotonics.9b01501
Perovskite	784	0.40	1.59	0.81	10.1364/OE.24.023677
InGaAs/GaAs	1030	1.50	1.21	1.76	10.1364/OPTICA.4.001468
InGaAs/InP	1370	1.80	0.91	1.19	10.1021/acs.nanolett.6b04690

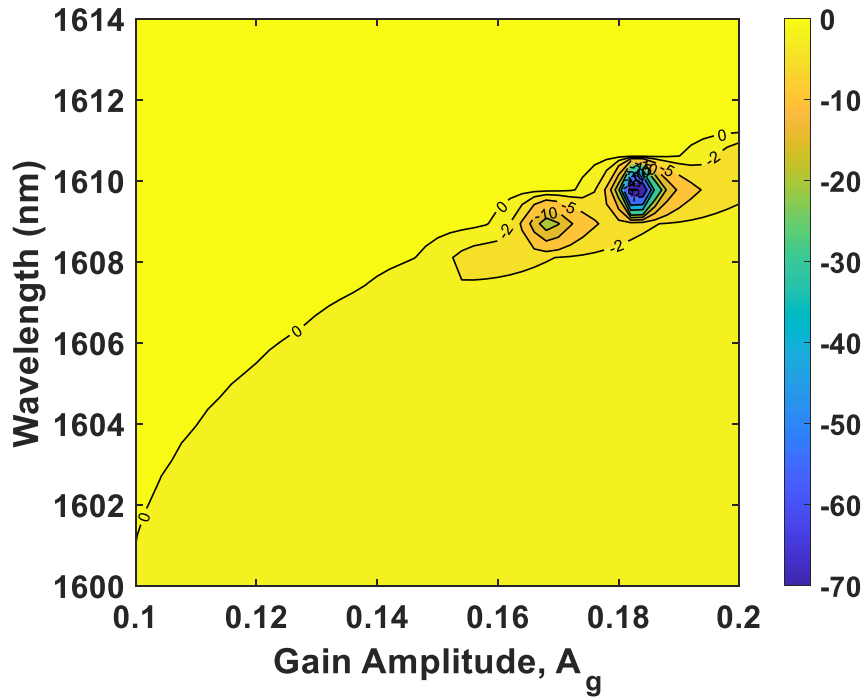
InP	925	1.60	1.34	2.33	10.1038/NPHOTON.2015.199
Organic Semiconductor	582	1.10	2.14	4.04	10.1038/s41598-019-47589-4
Organic Semiconductor	450	0.20	2.76	1.23	10.1038/s41528-019-0062-4
Organic Semiconductor	576	0.40	2.16	1.50	10.1038/s41528-019-0062-4
Organic Semiconductor	676	0.30	1.84	0.82	10.1038/s41528-019-0062-4
Organic Semiconductor	590	0.13	2.11	0.46	10.1038/s41467-019-11336-0
PbS QDs	1641	3.38	0.76	1.56	NA
PbS QDs	1649	2.10	0.75	0.96	NA
PbS QDs	1629	1.80	0.76	0.84	NA
PbS QDs	1588	3.40	0.78	1.68	NA
PbS QDs	1593	3.60	0.78	1.77	NA
PbS QDs	1600	2.90	0.78	1.41	NA
PbS QDs	1547	3.80	0.80	1.98	NA
PbS QDs	1566	5.38	0.79	2.74	NA
PbS QDs	1571	4.18	0.79	2.11	NA

Additionally we investigated into the mode structure of the measured spectra to as some lasers seemed to exhibit multi-modal behaviour and others appeared to operate with a single-mode. A selection of spectra were selected from the different DFB laser samples (3, 6, 9 and 10 in Table S2), with spectra varying from more obviously multi-modal (Fig. S5b & S5c) to single peaks (Fig. S5d). The width of the fitted Lorentzians was shared for each spectral fitting. These spectra were then fitted with 3-5 Lorentzians was shared width.



**Supplementary Figure 5. Lorentzian Fittings to Laser Spectra.** Raw lasing spectra is fitted to a sum of 3 – 5 Lorentzian peaks for (a) 5.4 nm CQDs lasing at 1570 nm, (b) 5.7 nm CQDs lasing at 1600 nm, (c) 6.0 nm CQDs lasing at 1641 nm, and (d) 6.0 nm CQDs lasing at 1649 nm. Each fitting shares the width parameter between the Lorentzians, the FWHM of which is displayed on each plot. Additionally the height of each individual Lorentzian is indicated in the legend.

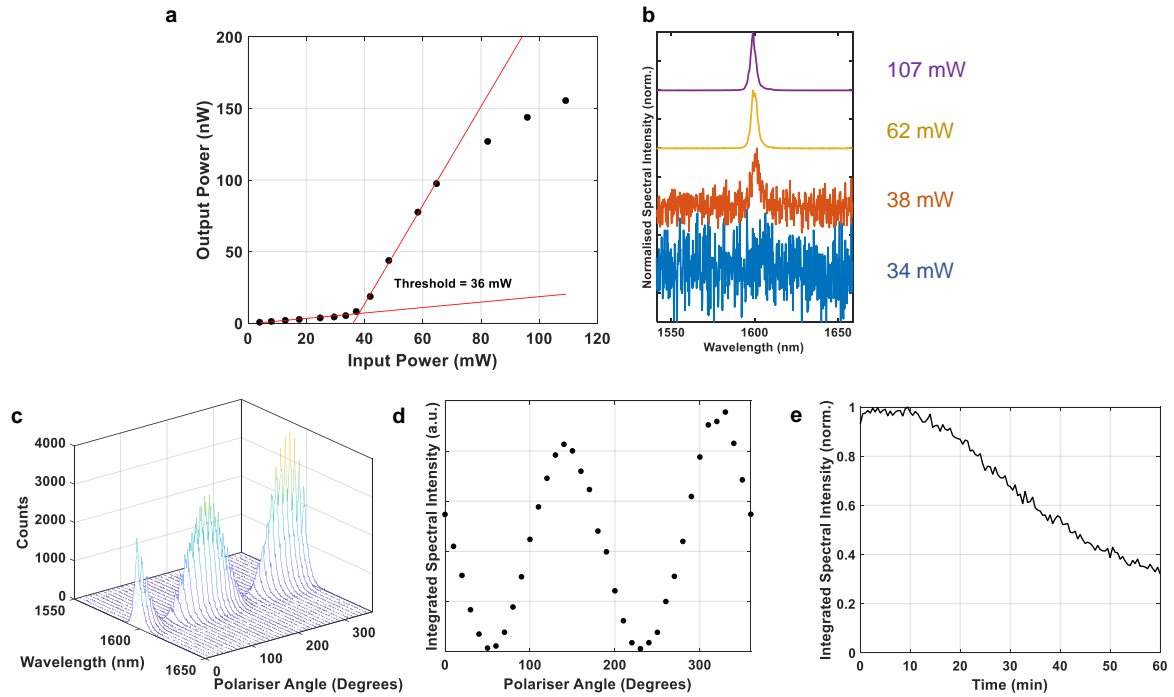
As can be seen, several Lorentzian (3-5) are needed to reproduce the lasing spectra. The width of an individual fitting was consistently ~ 2 nm suggesting that spectra with FWHM of 2 nm (lasers 8, 10 and 12 in Table S2) can be thought of as majority single-mode lasers with some scattering background. Additionally we can see from the variable gain FDFD model, that when lasing modes are detuned from peak gain (1600 nm) additional lasing modes are predicted.



**Supplementary Figure 6 Absorption from variable gain FDFD model for off resonant structure.** A contour plot of the simulated absorption of the rectangular structure and gain centred at 1600 nm. The transparency contour (absorption = 0) is indicated and areas of negative absorption indicates gain in the system. The structural parameter used were a period of 885 nm, a duty cycle of 0.45, a height of 55 nm, and a 90° side-wall angle  $\theta$ .

Fig. S6 shows the absorption as calculated using the same FDFD model as used in Fig. 1, but instead of a height of 40 nm, a height of 55 nm was used. As can be seen, this increase in height red shifts the lasing by 10 nm. As the resonance shifts away from the central gain wavelength (1600 nm), multiple lasing modes start to appear separated by 1 nm.

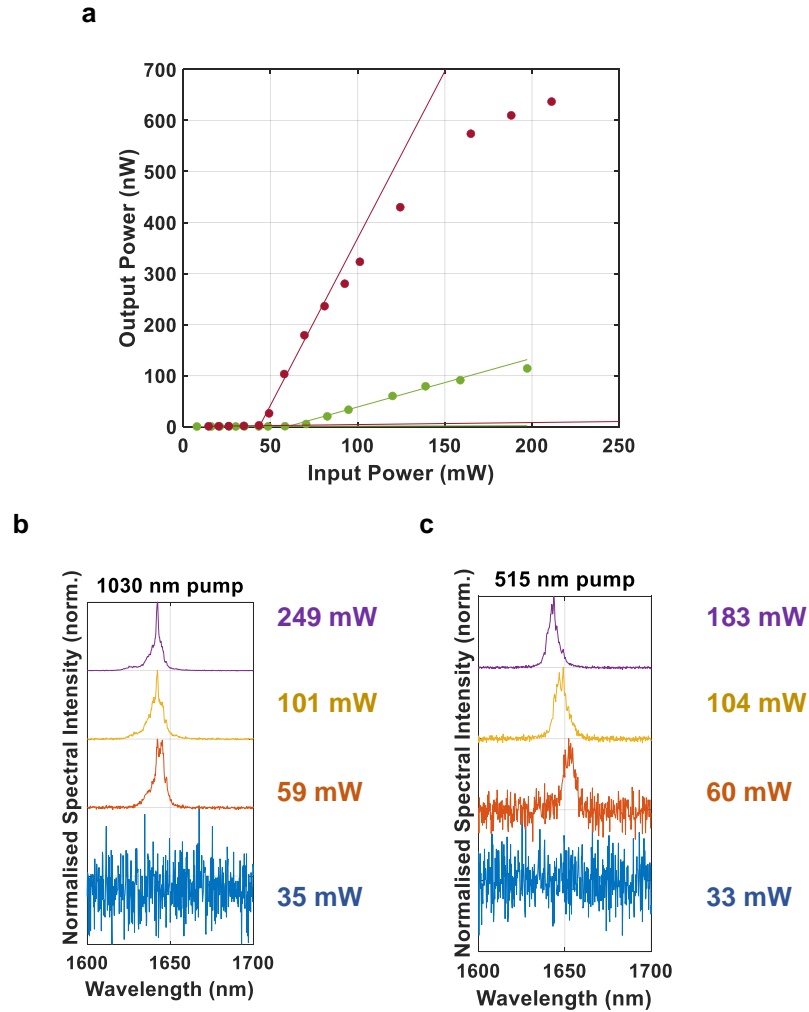
## V. DFB Characterisation



**Supplementary Figure 7. DFB Input/Output Power.** (a) Input/Output optical power measured from a PbS CQD DFB laser using 5.7 nm dots and a grating period of 880 nm. Threshold input power was extracted as the intersection of linear fits to be 36 mW which equates to a pump fluence of  $1045 \mu\text{J}/\text{cm}^2$ . (b) Spectra collected at 4 different indicated pump powers. (c) 1598 nm DFB lasing spectra collected through a linear polariser in a rotating mount. Spectra is plotted as a 3D waterfall as a function of the polarisers rotation angle. (d) Integrated spectral data from (c) plotted as a function of angle. Dotted lines indicate when the polariser is perpendicular and parallel to the grating direction. (e) Stability measurement of lasing at  $3000 \mu\text{J}/\text{cm}^2$  of pump fluence at a repetition rate of 50 kHz. The lasing intensity dropped to 50 % of its initial maximum after 40 minutes.

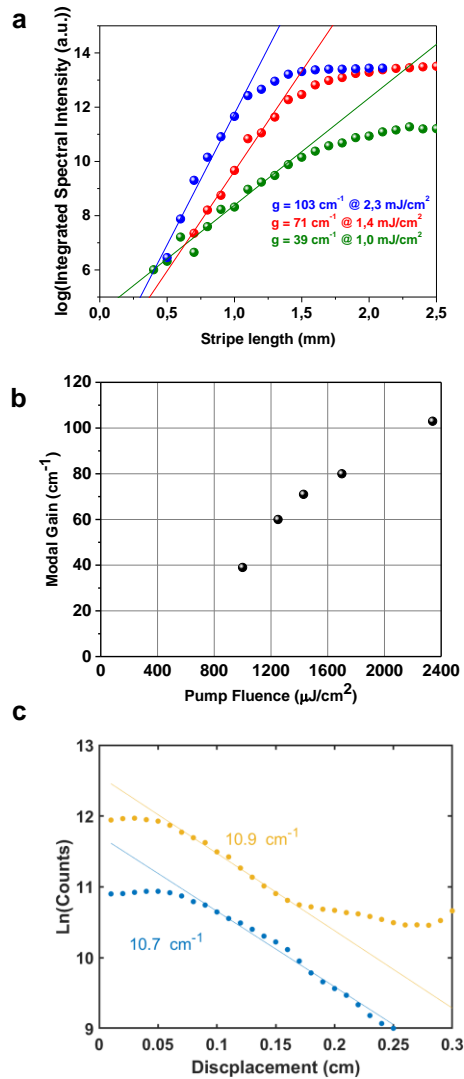
## VI. Comparison between infrared (1030 nm) and green (515 nm) pumping Conditions

We tested the doped PbS DFB sample under different pumping conditions. When pumping with 515 nm the lasing threshold increases from 410  $\mu\text{J}/\text{cm}^2$  to 560  $\mu\text{J}/\text{cm}^2$  and the line slope efficiency decreased by a factor of 6.5. Additionally, the spectrum broadens under 515 nm pumping and is seen to blue shift with increasing pump fluence. This blue shift is indicative of heating in the sample as was present when gratings were made out of  $\text{SiO}_2$ , meaning that the excess thermalization energy is no longer being dissipated by the  $\text{Al}_2\text{O}_3$  substrate.



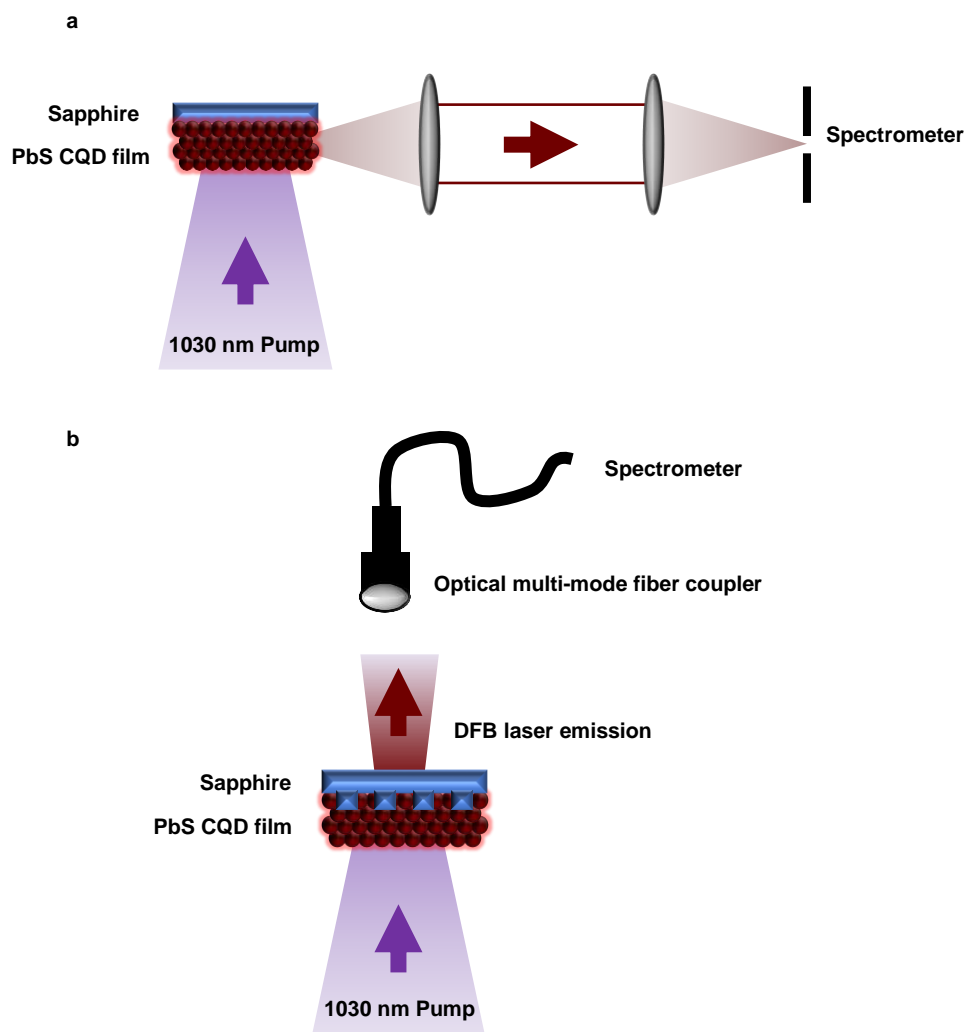
**Supplementary Figure 8. ASE Moving edge loss and variable stripe length.** (a) Input/Output power from doped 6.0 nm CQD DFB laser at 1642 nm using the fundamental 1030 nm infrared pump (red points) and the frequency doubled 515 nm output (green points). Linear fits were used to calculate the lasing threshold measured to be 43.3 mW (410  $\mu\text{J}/\text{cm}^2$ ) and 60 mW (560  $\mu\text{J}/\text{cm}^2$ ) respectively. Selected spectra using the (b) infrared pump laser and the (c) green pump laser.

## VII. Gain and Loss Measurements



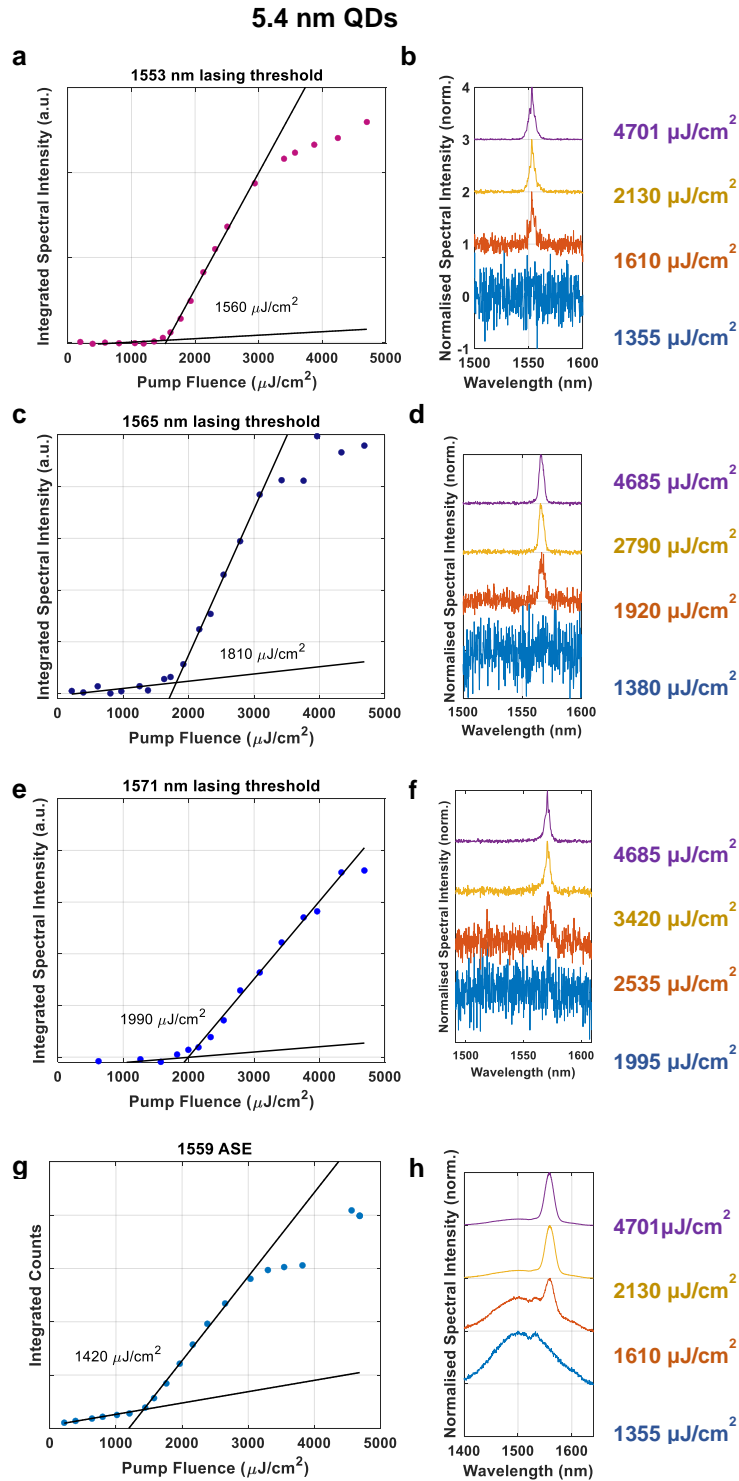
**Supplementary Figure 9. ASE Moving edge loss and variable stripe length.** (a) Variable stripe length experiments for three different pump fluences. Linear fits are used to extract the modal gain of the CQD films CQD modal gain as a function of pump fluence reaching a maximum of  $103 \text{ cm}^{-1}$ . (b) Measured modal gain plotted for five different pump fluences. (c) Moving edge loss showing the natural log of the integrated ASE spectrum as a function of displacement of the pump stripe from the edge of the film. Linear fits are used to extract the exponential decay of the signal and extract the waveguide loss of the CQD film in two different locations.

## VIII. Experimental Schematics



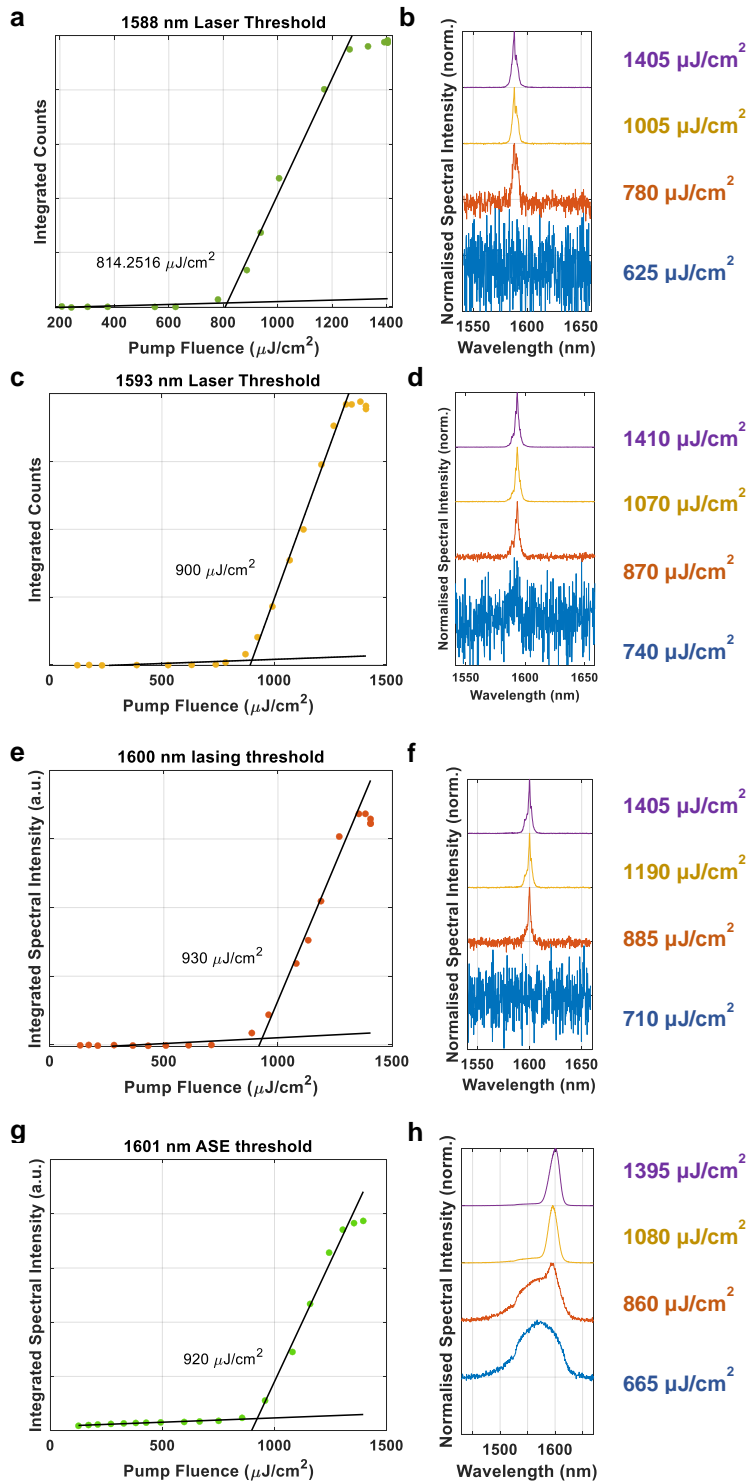
**Supplementary Figure 10. Experimental configurations.** Diagrams showing how spectra are collected for (a) amplified spontaneous emission, and (b) lasing.

## IX. Lasing Threshold Calculations and Spectral Data



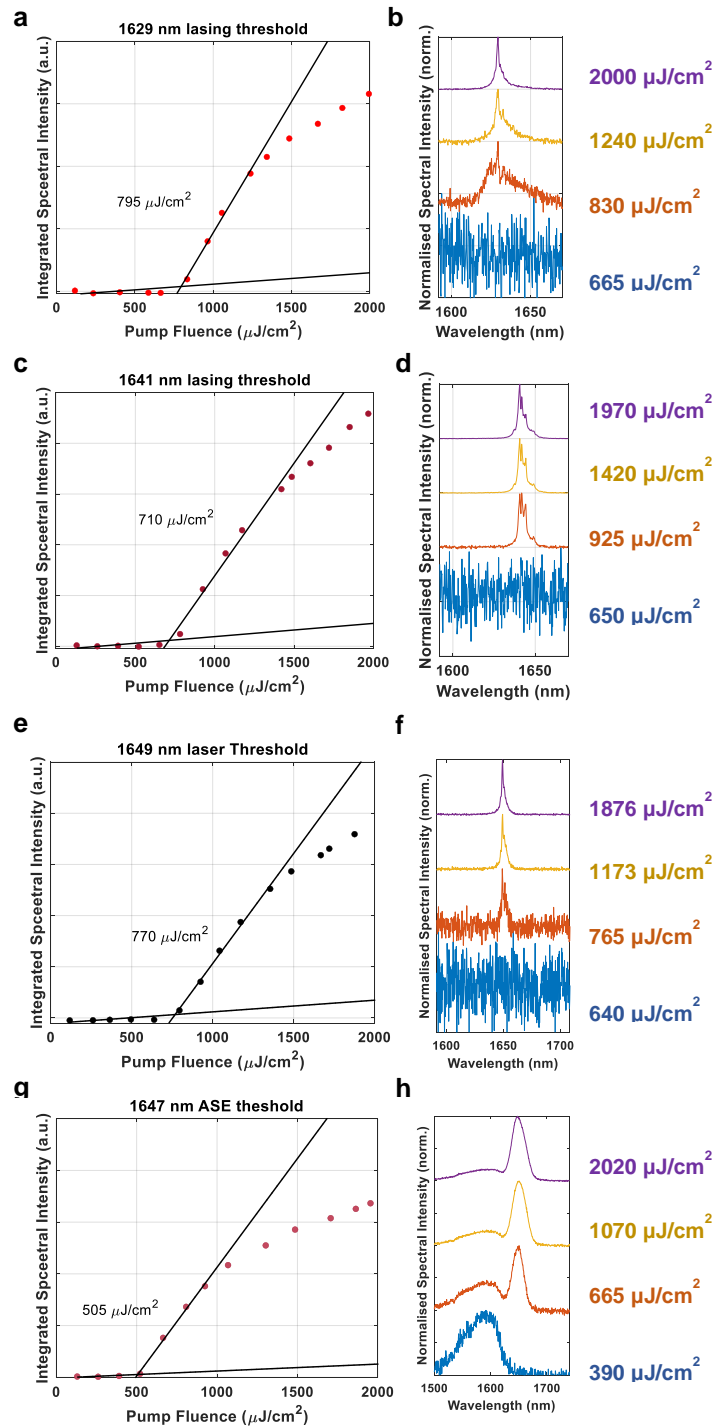
**Supplementary Figure 11. Threshold and spectral analysis from 5.4 nm CQD films.** Integrated spectral intensity plotted against incident pump fluence and sample spectra for the (a)-(b) 1553 nm, (c)-(d) 1565 nm, (e)-(f) 1571 nm DFB lasers and (g)-(h) the corresponding ASE analysis for 5.4 nm CQDs. Indicated thresholds were used to create Fig. 3(b).

### 5.7 nm



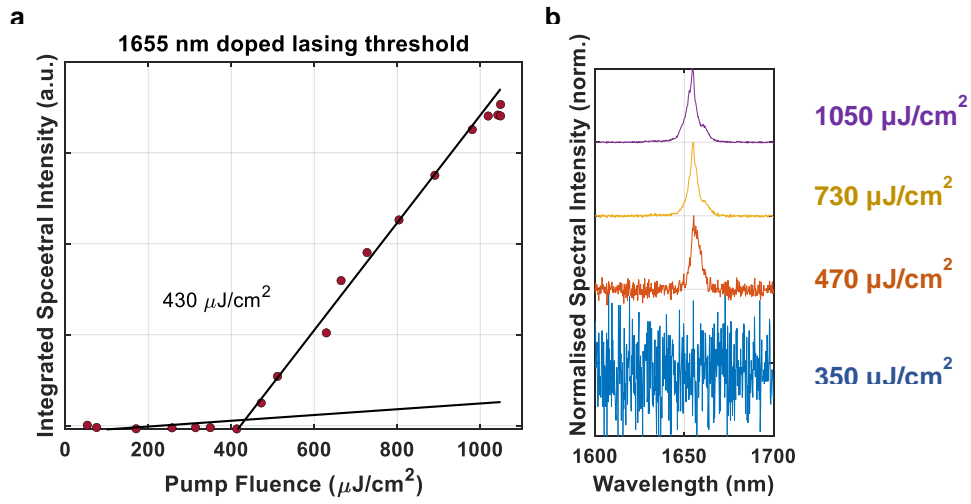
**Supplementary Figure 12. Threshold and spectral analysis for 5.7 nm CQD films.** Integrated spectral intensity plotted against incident pump fluence and sample spectra for the (a)-(b) 1588 nm, (c)-(d) 1593 nm, (e)-(f) 1600 nm DFB lasers and (g)-(h) the corresponding ASE analysis for 5.7 nm CQDs. Indicated thresholds were used to create Fig. 3(b).

### 6.0 nm



**Supplementary Figure 13. Threshold and spectral analysis for 6.0 nm CQD films.** Integrated spectral intensity plotted against incident pump fluence and sample spectra for the (a)-(b) 1629 nm, (c)-(d) 1641 nm, (e)-(f) 1649 nm DFB lasers and (g)-(h) the corresponding ASE analysis for 6.0 nm CQDs. Indicated thresholds were used to create Fig. 3(b).

### Doped 6.0 nm



**Supplementary Figure 14. Threshold and spectral analysis for doped 6.0 nm CQD films.** (a) Integrated spectral intensity plotted against incident pump fluence for the 1555 nm doped CQD DFB seen in Fig. 4(c) and (b) sample spectra at indicated pump.

Table S2 : Summary of all PbS DFB lasers fabricated

Laser no.	QD Diameter (nm)	Period (nm)	Wavelength (nm)	Energy (eV)	Effective Refractive Index	Threshold ( $\mu\text{J}/\text{cm}^2$ )	FWHM (nm)	FWHM (meV)	Doped	Location
1	5.4	850	1553	0.80	1.83	1560	3.8	2.0	No	Figure 3
2	5.4	855	1565	0.79	1.83	1810	5.4	2.8	No	Figure 3
3	5.4	860	1571	0.79	1.83	1990	4.2	2.1	No	Figure 3
4	5.7	875	1588	0.78	1.81	815	3.4	1.7	No	Figure 3
5	5.7	880	1593	0.78	1.81	900	3.6	1.8	No	Figure 2 & 3
6	5.7	885	1600	0.78	1.81	930	2.9	1.4	No	Figure 3
7	5.7	880	1598	0.78	1.82	1045	3.4	1.7	No	Figure S7
8	6.0	910	1629	0.76	1.79	795	1.7	0.9	No	Figure 3
9	6.0	915	1641	0.76	1.79	710	3.4	1.6	No	Figure 3
10	6.0	920	1649	0.75	1.79	770	2.1	1.0	No	Figure 3 & 4
11	6.0	915	1655	0.75	1.81	430	4.8	2.2	Yes	Figure 4
12	6.0	920	1642	0.76	1.78	410	2.1	1.0	Yes	Figure S8

## X. Duty Cycle Discussion

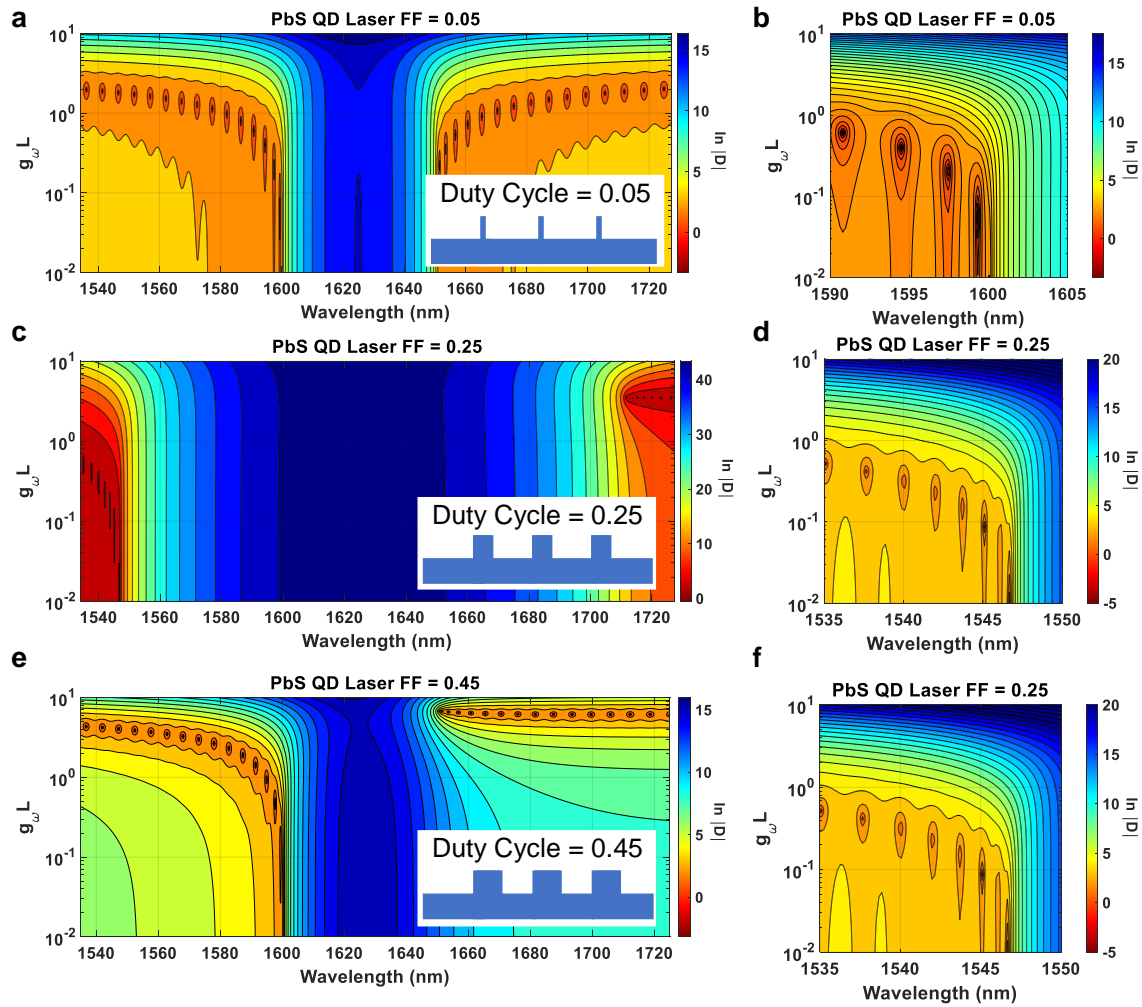
To aid our choice of what duty cycle to use in this work we calculate the DFB mode structure using coupled-mode theory as described by Kazarinov and Henry<sup>1</sup>. Below in Fig. S15 contours of the quantity  $\ln(D)$  are plotted, where  $D$  is the denominating factor in the equation for the DFB cavity reflectivity,  $R$  (i.e.  $R \propto 1/D$ ).

$$D \equiv \gamma L \cosh \gamma L - (g_\omega - i\Delta\beta - \kappa_r)L \sinh \gamma L \quad \text{Equation S1}$$

where

$$\gamma^2 = (g_\omega - i\Delta\beta - \kappa_r)^2 - (i\kappa_f - \kappa_r)^2 \quad \text{Equation S2}$$

$D$  is a complex surface which has an infinite series of complex roots for certain values of  $g_\omega$  and  $\Delta\beta$  (respectively the modal gain and propagation constant detuning) where  $D \rightarrow 0$  and therefore  $R \rightarrow \infty$ . These locations therefore provide high reflectivity for lasing modes. The surface is parameterised by the length of the cavity  $L$ , and the feedback and radiative coupling coefficients  $\kappa_f$  and  $\kappa_r$  respectively. The detuning,  $\Delta\beta$  can be directly converted into wavelength, as plotted in the Fig. S15. The y-axis of these contour plots are in the unitless quantity  $g_\omega L$ . From these contours we can see the spectral locations of the lasing cavity modes and their respective modal gain.

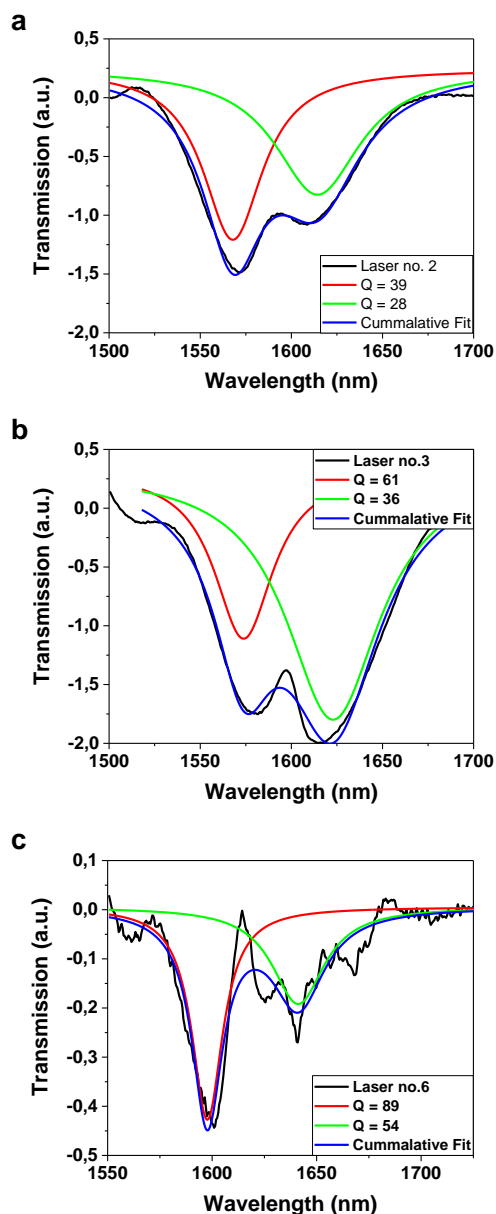


**Supplementary Figure 15. Coupled-mode theory results.** Counter plots of  $\ln(D)$  are presented in (a), (c) and (e) with the corresponding duty cycle for each case depicted as insets. (b), (d) and (f) show the same data as presented in (a), (c) and (e) respectively for a smaller range of wavelengths. The chosen duty cycles for study were (a) - (b) 0.05, (c) - (d) 0.25 and (e) - (f) 0.45. The central Bragg wavelength was chosen to be 1625 nm. To calculate  $\kappa_f$  and  $\kappa_r$ , the refractive index contrast between gain medium and grating material used was  $\Delta n = 0.8$ . the film thickness 130 nm and the grating height was 40 nm.

Considering a PbS CQD laser, with a Bragg condition centred at 1625 nm and a refractive index difference between the gain medium and the grating,  $\Delta n = 0.8$ , we can see low-threshold lasing modes at 1600 nm for duty cycles of 0.45 and 0.05; a 25 nm difference from the central Bragg condition (1625 nm). However, for a duty cycle of 0.25 the first low-threshold lasing mode occurs at 1545 nm, an 80 nm shift from the central Bragg condition. Despite the modal gain of this mode being the lowest, a duty cycle of 0.45 was chosen as this exhibited a higher gain discrimination between the first two lasing modes and the small bandgap would provide near-normal surface emitting lasers.

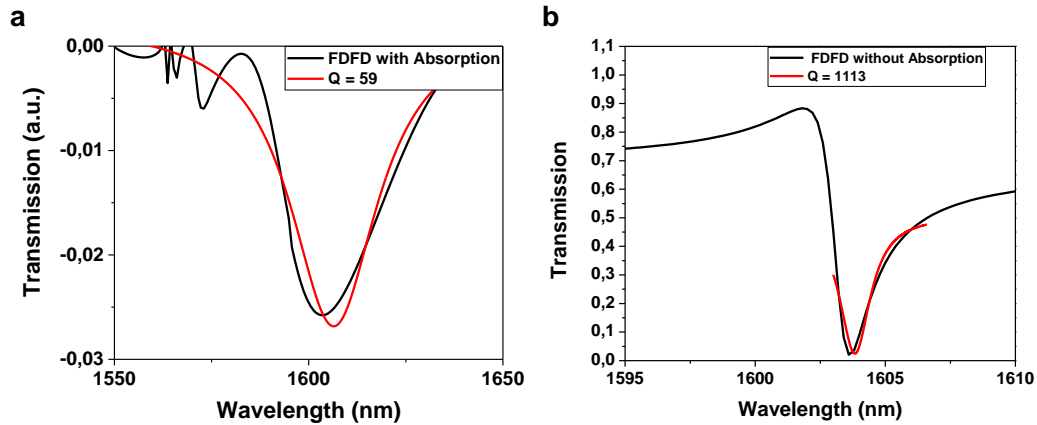
## XI. Discussion on Q-factor

Cold cavity Q factors were extracted from FTIR transmission data for laser samples 2, 3 and 6. The background of the transmission was removed using a spline fitting as presented in Figure S16. Two transmission resonances can be seen in the data corresponding to the low and high energy band edges separated by a roughly 50 nm bandgap, in good agreement with the results presented in Fig S15. A double Lorentzian was used to fit the data and the low energy resonance was extracted as the Q-factor of the laser cavity, where lasing is predicted and measured to occur. For these three samples the Q factors are measured to be 39, 61 and 89 respectively. Other samples could not be measured as their resonance overlapped with the exciton absorption, making the cold cavity resonance immeasurable.



**Supplementary Figure 16. Q-factor calculation from FTIR Transmission.** Black lines show the background corrected FTIR transmission data for laser samples (a) no. 2 (b) no. 3 and (c) no. 6. Red and green lines show the individual Lorentzian fits of the two band edges with the sum of the two shown in blue.

To shed light on the origin of the low Q factors of our samples further simulations were performed. The most obvious reasons for these low Q factors is the high self-absorption losses in PbS CQDs in the ground state. Figure S17(a) shows the background corrected transmission as calculated by FDFD (as described in Fig 2(a)), with an extracted Q-factor of the DFB resonance of 59. When the same simulation is run with the extinction coefficient set to zero (i.e. no material absorption) a sharp resonance appears and the Q factor increases  $> 1000$ . This identifies the self-absorption as a primary limiting factor of the low measured Q-factor. One further limitation to these low Q factors is the high refractive index contrast  $\Delta n$  between at the grating interface. DFB feedback coefficient  $\kappa_f$  is directly proportion to the refractive index contrast but the radiative coefficient  $\kappa_r$  is proportional to that of the square<sup>2</sup> ( $\kappa_f \propto \Delta n$ ,  $\kappa_r \propto \Delta n^2$ ). This therefore leads to a lossier cavity for high values of  $\Delta n$ .



**Supplementary Figure 17. Q-factor calculation from FDFD simulations.** (a) Background correct transmission of structure simulated in Fig 2(a) with a lorentzian fit to calculate the indicated Q-factor. (b) Transmission graph of the same simulated structure as in (a) but with the extinction coefficient set to zero and indicated Q-factor.

## References

1. Kazarinov, R. F. & Henry, C. H. Second-Order Distributed Feedback Lasers with Mode Selection Provided by First-Order Radiation Losses. *IEEE J. Quantum Electron.* **21**, 144–150 (1985).
2. Martins, E. R. *et al.* Low-Threshold Nanoimprinted Lasers Using Substructured Gratings for Control of Distributed Feedback. *Adv. Opt. Mater.* **1**, 563–566 (2013).